Journal Pre-proof

All-perfluoropolymer, nonlinear stability-assisted monolithic surface combines topology-specific superwettability with ultradurability

Wanbo Li, Chiuwing Chan, Zeyu Li, Sin-Yung Siu, Siyu Chen, Han Sun, Zeyu Liu, Yisu Wang, Chong Hu, Nicola Maria Pugno, Richard N. Zare, Hongkai Wu, Kangning Ren

PII: S2666-6758(23)00017-6

DOI: https://doi.org/10.1016/j.xinn.2023.100389

Reference: XINN 100389

To appear in: *The Innovation*

Received Date: 18 November 2022

Revised Date: 3 February 2023

Accepted Date: 5 February 2023

Please cite this article as: Li, W., Chan, C., Li, Z., Siu, S.-Y., Chen, S., Sun, H., Liu, Z., Wang, Y., Hu, C., Pugno, N.M., Zare, R.N., Wu, H., Ren, K., All-perfluoropolymer, nonlinear stability-assisted monolithic surface combines topology-specific superwettability with ultradurability, *The Innovation* (2023), doi: https://doi.org/10.1016/j.xinn.2023.100389.

PUBLIC SUMMARY

- The monolithic perfluoropolymer surface (MPS) strategy enables biomimetic surfaces to combine geometric-material mechanics with topology-specific superwetting stability.
- The theoretical model predicted optimal structures and materials to realize simultaneously superwettability and ultradurability.
- The stability of the biomimetic surfaces was extended into a nonlinear range for further improving ultradurability.
- The MPS strategy helps to translate bioinspired surface principles into real-world applications.

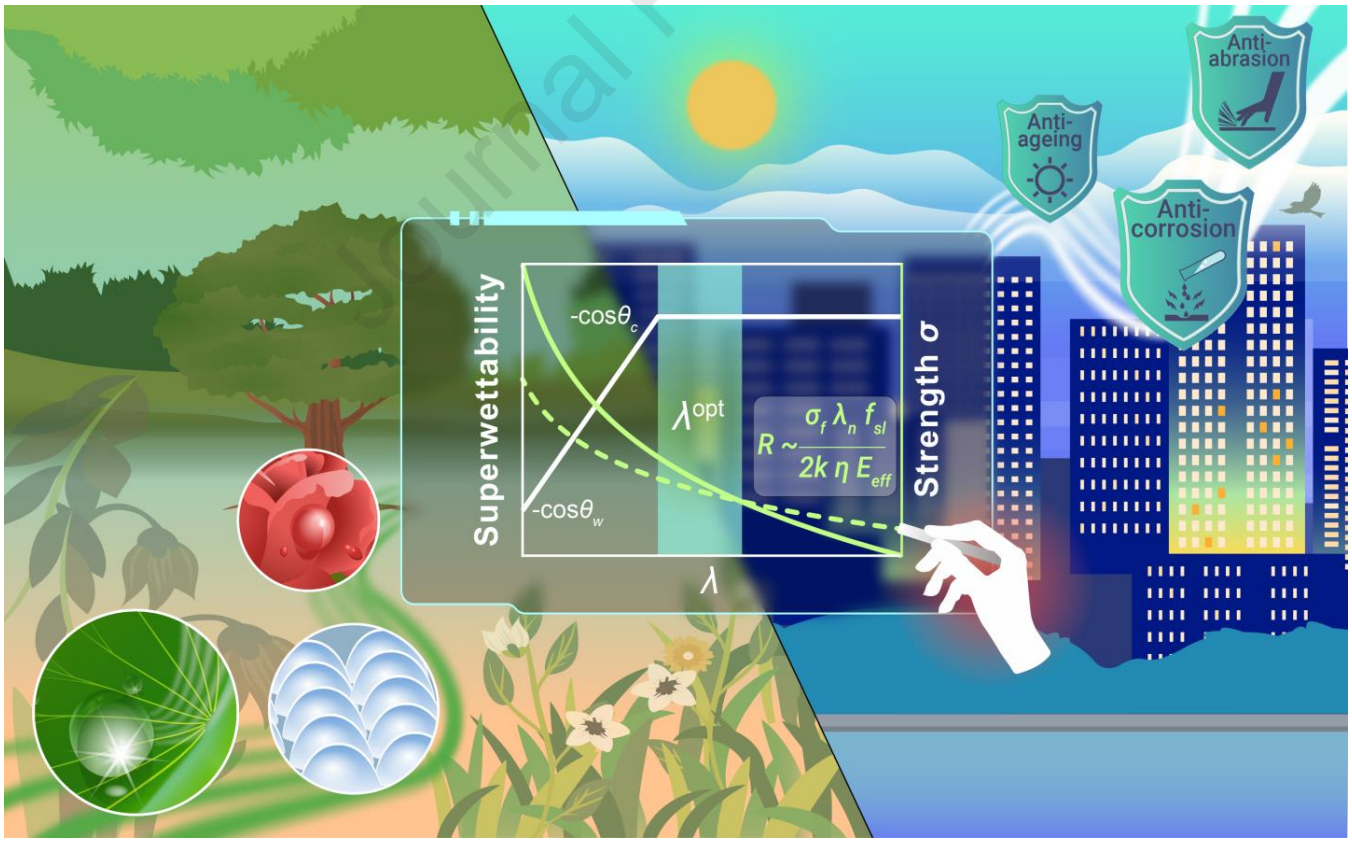

All-perfluoropolymer, nonlinear stability-assisted monolithic surface combines topology-specific superwettability with ultradurability

Wanbo Li,[1,6] Chiuwing Chan,[1] Zeyu Li,[1] Sin-Yung Siu,[1] Siyu Chen,[1] Han Sun,[1] Zeyu Liu,[2] Yisu Wang,[1] Chong Hu,[1] Nicola Maria Pugno,[3,4] Richard N. Zare,[5] Hongkai Wu,[2,*] and Kangning Ren[1,7,8,*]

[1]Department of Chemistry, Hong Kong Baptist University, Hong Kong 999077, China

[2]Department of Chemistry, The Hong Kong University of Science and Technology, Hong Kong 999077, China

[3]Laboratory of Bio-Inspired, Bionic, Nano, Meta Materials & Mechanics, Department of Civil, Environmental and Mechanical Engineering, Università di Trento, Trento 38100, Italy

[4]School of Engineering and Materials Science, Queen Mary University of London, London, UK, E1 4NS

[5]Department of Chemistry, Stanford University, Stanford, California 94305, USA

[6]School of Mechanical Engineering, Shanghai Jiao Tong University, Shanghai 200240, China

[7]State Key Laboratory of Environmental and Biological Analysis, Hong Kong Baptist University, Hong Kong SAR 999077, China

[8]HKBU Institute of Research and Continuing Education, Shenzhen 518057, China

* Correspondence：chhkwu@ust.hk (H.W.)； kangningren@hkbu.edu.hk (K.R.)

ABSTRACT

Developing versatile and robust surfaces that mimic the skins of living beings to regulate air/liquid/solid matter is critical for many bioinspired applications. Despite notable achievements, such as in the case of developing robust superhydrophobic surfaces, it remains elusive to realize simultaneously topology-

specific superwettability and multipronged durability owing to their inherent tradeoff and the lacking of a scalable fabrication method. Here, we present a largely unexplored strategy of preparing an all-perfluoropolymer (Teflon), nonlinear stability-assisted monolithic surface for efficient regulating matters. The key to achieving topology-specific superwettability and multilevel durability is the geometric-material mechanics design coupling superwettability stability and mechanical strength. The versatility of the surface is evidenced by its manufacturing feasibility, multiple-use modes (coating, membrane, and adhesive tape), long-term air trapping in 9-m-deep water, low-fouling droplet transportation, and self-cleaning of nanodirt. We also demonstrate its multilevel durability, including strong substrate adhesion, mechanical robustness, and chemical stability, all of which are needed for real-world applications.

INTRODUCTION

In nature, biological superhydrophobic skins often possess unique 3D microscale topologies that enable different specific interfacial functions for controlling surface matters.[1] A few examples include the nanopillar arrays on Cicada wings that promote transparency, self-cleaning, and mechanically rupturing cells,[2] the double reentrants on a springtail skin minimizing organic liquid wetting;[3] and the micro-papillae on a rose petal stabilizing water droplets at Wenzel wetting state.[4] For more examples, see Table S1. The exploration of these biological surfaces has inspired diverse topological functionalities – e.g., liquid detachment/adhesion,[5-9] gas entrapment,[10-12] anti-icing,[13-15] chemical shielding,[16] drag reduction,[17,18] oil/water separation,[19,20] heat transfer improvement,[21] and anti-bacteria activity.[22,23] While notable progress has been achieved in developing some biomimetic surfaces, such as in the case of superhydrophobic surfaces, there remains a major challenge to simultaneously control precise specific topology and realize the robustness of those biomimetic surfaces. In general, biomimetic surface functions require two essential components,[19,21,24-28] the specific 3D surface topologies and the surface chemistry of materials. However, both components are highly susceptible to material failure caused by stress concentration, short penetration distance for invasive matters, and the easy change of surface nature from hydrophobic to hydrophilic. Also, the need to construct the specific 3D architecture[29-34] recalls sophisticated manufacturing and limits material and structural options for enhancing robustness.

Recent years saw extensive efforts in translating bioinspired surfaces into real-world applications. For example, the surface robustness can be enhanced by introducing high-modulus materials[24,25,28,35,36] and perfluorinated chemistry[26,27,37] as manifested by those synthetic surface coatings. Yet, such coatings are commonly composed of disordered particles without microtopological controllability. Alternatively, "armor" structures (e.g., interconnected frames[29,38] and pillars[30,39]) can be micromachined to protect weak nanostructures. But this strategy is specific to structural geometry and rigidity. To date, it remains an

unresolved problem to develop versatile and scalable surfaces that simultaneously enable topology-specific functionality and ultradurability.[40]

Here, we present a nonlinear stability-assisted, monolithic perfluoropolymer surface (MPS) strategy to address the above challenge. In particular, MPS uses soft perfluoropolymers (sometimes referred to as Teflon, a commercial brand name) to make the entire coating, with all surface structures being part of this inert continuum. Using theoretical modeling and experimental validation, we found the MPS strategy combines geometric-material mechanics with superwetting stability well and suggests 1) an optimal structural design and preferential materials to simultaneously realize wetting and mechanical stability and 2) the extension of the stability of the biomimetic surfaces into a nonlinear range. This principle is contrary to conventional wisdom – using highly rigid structures to bear the concentrated stress yet failing once slight inelastic deformation occurs. MPS was prepared in multiple-use models (coating, tape, and self-supporting film) through a modified high-temperature imprinting approach which is low-cost and scalable. We also demonstrated the versatility of MPS for efficiently regulating surface matter, as well as multilevel durability.

RESULTS

Surface design and fabrication

The MPS strategy is shown in Fig. 1 and Supplementary Fig. S1. We design all the surface structureparts of this monolithic continuum which are firmly bonded to substrates without using any glue (Fig. 1A). The geometric mechanics of soft material is explored to improve the durability of biomimetic surfaces (Fig. 1B-D). We first consider the mechanical stability of MPS with structural hierarchy *n* from three mechanical failure mechanisms: (i) friction-driven bending, (ii) elastic instability, and (iii) crushing of a hierarchical structure (see Supplementary Text 1 for the details). Our modeling suggests that for a

preferential material with low friction coefficient μ, moderate Young's modulus E, and high failure strength σ_f, the key to reaching mechanical robustness is to fulfill a geometric rule, that is, the structure slenderness λ_n' achieves the same resistance for mechanisms (i) and (ii) when

$$\lambda_n' \sim \frac{\pi^2 E\mu}{2\sigma_f}$$

Moreover, when considering the wetting stability for MPS from the energy perspective,[41,42] a water droplet with a lower Gibbs free energy than the Wenzel wetting mode can be stabilized at the Cassie-Baxter state only for a slenderness larger than the critical value

$$\lambda_n'' = \frac{1-f_{sl}}{f_{sl}}\frac{1+\cos\theta_Y}{\cos\theta_Y}$$

where θ_Y and f_{sl} are the Young's contact angle and the pillar area fraction of the surface, respectively By coupling the evolution trends for maximizing mechanical strength and stabilizing water repellency at the Cassie-Baxter state, the optimal slenderness λ_n^{opt}emerges between λ_n' and λ_n'', that is, this is achieved when $6 \leq \lambda_n^{opt} \leq 8.5$ (Fig.1B). As a result, when the wetting property is measured and the material is tough, it is found that the surface is highly abrasion-resistant (Fig. 1C).

One essential part of our design is that the nonlinear dynamics of tough microstructures could be leveraged to strengthen mechanical robustness. As shown in Fig.1D, the tolerable compressive pressure of structures without losing wetting stability is much greater than the material failure strength using elastic deformation as the boundary condition, leading to an elevated resistance to crushing failure, with a robustness factor R being defined as

$$R \sim \frac{\sigma_f \lambda_n f_{sl}}{2k\eta E_{eff}}$$

where k is a constant on the order of the unity, η is the compaction index, $and\ E_{eff}$ is the effective Young's modulus (see mechanism (iii) in Supplementary Text 1 for the details). Such a geometry-based nonlinear mechanical behavior is also observed for many biological structures[43,44] and is counterintuitive to the common assumption that the biomimetic topological surfaces fail once inelastic deformation occurs. In the control experiments, this nonlinear regime collapses into the conventional one when the material toughness is reduced, that is, for structures made of materials with high hardness and large slenderness, fracture took place at the bottom and caused the immediate loss of preferential wettability (Fig.S1).

Following the MPS design, we chose perfluoropolymer (MFA F1540, Solvay company) as the base material and developed a 3D high-temperature soft imprinting method to thermally fuse it (Supplementary text 2) with the substrate and create rational 3D microstructures on it (Fig. 2A). The key to the method is a silicone thermal mold that possesses configurable elasticity and shape memory at extremely high temperatures (up to 350 °C). Usually, such properties of normal silicones degrade rapidly owing to the scission of flexible molecular chains when heated.[36,45] To suppress degradation at elevated temperatures, we used iron nanoparticles to avoid the oligomer formation by binding the oxide's surface hydroxyl groups with silanol groups in the silicone mold, which also serves as soft crosslinks that maintain flexibility (Supplementary text 3 and Supplementary Fig. S2). In this way, we produced thousands of MPS products from one soft mold with improved fidelity within a short time (5 min per cycle). The products include transparent MPS coatings on different substrates (e.g., glass, fabric, polyimide, and aluminum), self-supporting and flexible films, and tapes (Fig. 2B-D and Supplementary Fig. S3). Such versatility makes MPS adaptive to different substrate and dynamic deformations. Collectively, the MPS strategy shows the promise of scalable and versatile biomimetic surfaces with topology-specific functionality and multipronged robustness.

Some topology-specific functions

In what follows, we demonstrate three examples of MPS for efficient regulating of air/liquid/solid matters (Fig. 3 and supplementary Fig. S4). Although the surfaces commonly manifest two-tier structures in micro and nano scale, their wettability such as water contact angle θ^*, roll-off angle $\theta_{roll\text{-}off}$, droplet adhesion, pressure stability, and restitution coefficient can be very different (see Supplementary Text 4 for details), and thus manifesting preferential yet strong superwettabilities. The first example is an air-trapping coating inspired by the springtail's skin (Fig. 3A). As shown in Fig. 3B and 3C, The MPS was imprinted with honeycomb cavity arrays with wetting resistance further strengthened by doubly reentrant edges. The sample could stably trap air in the cavities after being immersed under seawater with the extra pressure of ~90 KPa for 30 days, with a gas retention fraction φ ~ 92.7% (where φ is the volume ratio between the entrapped gas and the cavity). The extra pressure was equivalent to that in ~9-meter-deep water (Fig.3D), beyond the draft range of most ships. While the air-trapping surface could reduce the drag of marine vehicles, the inertness and anti-stickiness of perfluoropolymer endow the coating with enhanced corrosion and aging resistance, reduced microorganism adhesion, and outstanding robustness against cleaning operations. In addition, the reentrants can also be constructed on the top of an array of pillars, which made MPS effectively repellent to low-surface-energy liquids (Supplementary Fig. S5).

The second example is a rose petal-mimicking surface for a low-fouling droplet transfer (Fig. 3E-H). While prior works proposed the operation mechanism of adhesion-based droplet transfer, the functional application is still limited by the low sample compatibility and sample loss during transport caused by surface fouling, microdroplet residuals, and poor chemical tolerance. We conducted experiments to evaluate the MPS with regard to these challenges. As shown in Fig. 3G, Supplementary Fig. S6, and Supplementary Video S1, a broad range of liquids (e.g., serum, cell culture medium, and even 1-M NaOH) were compatible with our MPS, and minimal sample fouling was observed during transport, suggesting

the functional robustness and generality of the surface. Meanwhile, all control samples made of normal lab materials, such as polystyrene (PS) and polypropylene (PP) even after surface fluorination protection, showed noticeable fouling/sample loss (Fig. 3H). The observed difference between MPS and the control samples in droplet transfer performance could be attributed to two reasons. First, we design the structure edges of MPS to have convex micro-curvature, thus reduces the pinning effect to trigger capillary bridge rupturing,[46] whereas the previous report shows that structures with sharp edges inevitably pin microdroplets. Second, the MPS is a perfluoropolymer, which has a higher density of fluorine and mechanical stability than commonly-used monolayer fluorinated coatings, one of the best anti-fouling coatings in past reports. As a result, MPS will enable a lower level of molecular fouling and reduce the chance of leaving residue droplets,[47] as demonstrated by control experiments shown in Fig. 3H.

As a final example we mimic the lotus effect (Fig. 3I-M). A MPS containing hierarchical structures showed outstanding water repellence (Fig. 3L). Even after being placed in the outdoor environment for one month, MPS can self-clean against nano-sized dirt (one major component of ambient fine particulate matters[48]) by impacting water droplets[49] (Fig. 3M, Supplementary Fig. S7 and S8). In contrast, the control surfaces possessing the same topology but made from other materials failed to self-clean under the same conditions (Fig. 3M, Supplementary text 5, and Supplementary Video 2), demonstrating the rationale of our MPS design for improving self-cleaning performance.

Multilevel durability

We then evaluated the multilevel durability of MPS considering their mechanical strength (e.g., substrate adhesion, structural toughness), chemical resistance to solvents and reactive substances, and weathering durability against radiant, heat, and moisture. Considering the delicate structure and possibly least robustness among all the samples, we used the lotus-mimicking sample in these tests. First, a standard

shear-stress model recorded ~5.66 MPa substrate adhesion of our MPS, which was even stronger than 3M PR1500 (Fig. 4A), a strong and multi-purpose glue. The bonding was so strong that during detaching, the cracks took place in the MFA layer rather than at the bonding interface, as evidenced by the elementary composition (Fig. 4B), microscopic morphology, and wettability of the substrate surface (Supplementary Fig. S9). To cross-compare, we also performed the tape-peeling test frequently used in past reports.[26,29] Here we used a rubbery adhesive peeling test to upgrade the test. Though some commercial coatings could sustain certain cycles of tape peeling, rubbery adhesive peeling immediately reveal their insufficient bonding strength (Supplementary Fig. S10A). In sharp contrast, MPS did not present noticeable deterioration after thousands of rounds of tape peeling and hundreds of rubbery adhesive peeling. Moreover, our MPS is highly flexible – a MFA-glass fiber hybrid film passed more than 100,000-cycle folding (Supplementary Fig. S10 B-C).

We evaluated the structural strength of the coating using two models – crushing and abrasion (Supplementary Fig. S11). During the crushing test, our MPS did not show any noticeable change after exposure to 300 kPa loads, as plotted in Fig. 4C. When the load reached 500 kPa, the surface showed deteriorated hydrophobicity (θ^* ~154.6° and $\theta_{roll\text{-}off}$ ~10.8°). These pressures were far beyond the ground pressure of a human adult (~50 KPa), a military tank (~100 KPa), and an elephant (~250 KPa) (Fig. 4C). In the abrasion test, the surface of the MPS maintained water repellence over ~1500-cycle abrasions (Fig. 4D). As could be explained by our friction-bending model, the microstructures on the MPS surface will not be torn down. Instead, dense nano-sized hairs are continuously regenerated on the tops of the micropillars (supplementary Fig. S12), realizing a self-regeneration effect until the surface texture was worn away after ~1800-cycle abrasions. MPS also passed challenging tests mimicking real-world wearing conditions (Supplementary Video S3 and S4), illustrating our MPS materials' remarkable robustness. In

control experiments, all the samples commercial products and surface similar to the existing reports[50] lose superhydrophobicity simply after a few finger wipes (Supplementary Video 5).

Chemical resistance to corrosive vapors and aging was also tested. Distinguished from the conventional liquid immersion tests, we treated the samples with saturated corrosive vapors. We consider it a more meaningful test for the chemical robustness of a superhydrophobic coating, as the vapor can easily penetrate the air cushion to destroy the coating or even the underlying substrate. We found MPS can survive various corrosive gas/vapor (e.g., strong acid, alkali, oxidant, and organic solvent) for more than 7 Days (Fig. 4E). Moreover, in an accelerated aging test, MPS did not show any noticeable decay in water repellency throughout this entire test, indicating its prolonged lifespan in real-world weathering. In sharp contrast, control samples turned hydrophilic within one day (Fig. 4F, Supplementary Fig. S13, and Supplementary Video 6). We also tested our coatings under even harsher conditions which can appear in many situations in industrial, high altitude, and even space environments. These test conditions include sonication in strong chemicals listed in Fig. 4E, exposure to 185-nm UV radiation for 7 days, and heating at 200 °C for 7 days (Supplementary Fig. S14). The MPS remained intact after all these tests.

DISCUSSION

The advantages of MPS over superhydrophobic surfaces produced by conventional strategies (see Table S2 for the details) are summarized using some qualitative evaluation indices in a radar map (Fig. 5). The details of the rubrics are presented in Table S3). The MPS achieved performances comparable to best records in multiple aspects, *e.g.*, peeling, abrasion, crushing, and chemical/aging resistance. Also, MPS favors eco-friendliness by minimizing the release of microplastics and nanomaterials, which is impossible for those nanoparticle-based coatings. Moreover, the fabrication cost of the MPS strategy (estimated at within 10 $\$/m^2$) is competitive, especially considering its capability to create large-scale arrays of precisely defined true-3D microstructures and outstanding durability. Altogether, the MPS

strategy has demonstrated the capability to simultaneously realize topology-specific functionality and multilevel robustness for the control of gas/liquid/solid matters, which may fulfill the challenging requirements for real-world applications in air trapping, liquid transport, and self-cleaning, as well as many other possible applications such as anti-icing, anti-corrosion, heat transfer, and drag reduction.

MATERIALS AND METHODS

Test the stabilities of the soft pillars

For validating the theoretical prediction, the mechanical strength of pillars (λ ~8, f_{sl} ~10%) against abrasion, pressing, and buckling were tested. For the abrasion test, the pillar array (2×2 cm^2) was brought into contact with a 1200-Cw sandpaper, and a weight of 100 g was applied. The sample was pushed forward 10 cm along the ruler and then backward to the original point. Then the sample was rotated by 90°, and the movement was repeated. This procedure is defined as one abrasion cycle. The cycle was repeated to test the sample's abrasion robustness. For the press test, fixed loads (from 0 to 16 MPa) were applied on the samples (1×1 cm^2) for 10 min. After the abrasion and pressing tests, the pillar geometries (i.e., pillar length *l*, pillar diameter *D*, and center-to-center distance *d*) were characterized with SEM. The Cassie-Baxter theory suggests that, for the pillar array with an inherent water contact angle θ_Y ~110°, f_{sl} must be lower than 20% to allow $\theta^* \geq 150°$. Thus, pillars that have $f_{sl} > 20\%$ were considered lost superhydrophobicity. For comparison, polypropylene (PP) and polystyrene (PS) samples with the same surface architecture were also tested.

Fabrication of MPS

The MPS was fabricated by thermally bonding perfluoropolymer on substrates (*e.g.*, glass, textile, polyimide (PI), and aluminum plate) and imprinting 3D structures onto the surface. For bonding perfluoropolymer with a substrate, perfluorinated polymers (*e.g.*, MFA F1540, Solvay company) were

laminated with the substrates at 350 °C for 10 min, and then cooled to 200 °C, with the pressure maintained at 0.5 MPa (See Supplementary Text 2 for details). After that, the perfluoropolymer layer on the substrate was textured using 3D imprinting as described below.

Before the 3D imprinting process, master structures with predesigned texture were fabricated by 3D printing. To prepare for the 3D imprinting, a thermally stable mold was cast from the master (for details, see Fig.S2); then, the perfluoropolymer layer on the substrate was imprinted by the thermal mold at 280 °C for 1 min under 0.1 MPa MPS was finally collected after cooling to room temperature. Both the master and the soft mold could be reused for scalable manufacturing.

MPS in different use modes, i.e., coatings, membranes, and adhesive tapes were fabricated as illustrated in Supplementary Fig. S3. For producing the self-supporting MPS membrane, a perfluoropolymer film is directly imprinted. For producing the adhesive tape, MPS was first fabricated on a polyimide (PI) film and then an adhesive is coated on the other side of the PI film.

Characterization of the hydrophobicity

The hydrophobicity of the materials was characterized by measuring the static water contact angle (θ^*) and the roll-off angle ($\theta_{roll\text{-}off}$). To characterize θ^*, the optical image of a 5-μL water droplet on a horizontal surface was taken, and then the angle within the liquid body between the liquid-gas and liquid-solid lines was measured. To characterize $\theta_{roll\text{-}off}$, a 10-μL droplet was placed on the horizontal surface and the sample surface was tilted gradually at a resolution of 0.1°. The critical angle that enables the droplet to start rolling was recorded as $\theta_{roll\text{-}off}$. In each case, five replicates of each measurement were performed to calculate the standard deviation.

Air trapping

To test the trapping performance, the samples were immersed in seawater and the air bubbles trapped inside the sample surface were photographed with an optical microscope. To evaluate the trapping

efficiency, the sample immersed in water was placed in a sealed container, which was then pressurized to different pressures (0, 20, 40, 60, 80, and 90 KPa compared to normal pressure) for 24 hours. Optical images were taken afterwards and analyzed using ImageJ software (U.S. National Institutes of Health). The trapping efficiency was defined as the volume ratio between the air retentate and the cavities.

Droplet transportation

To test the transportation, a liquid droplet was firstly placed on a low-adhesion superhydrophobic surface, and was then captured by a high-adhesion surface upside down; finally, the droplet was transported to another high-adhesion MPS surface. To demonstrate the anti-corrosion capability, a droplet of 1-M NaOH was employed. To demonstrate the anti-fouling performance, a droplet of fluorescently labeled globulin solution was adhered on the high-adhesion surface upside down for 30 min, and then transported to another high-adhesion surface, after which, a fluorescence image was taken to identify the fouled area. The fouling ratio was defined as the projected area ratio between the fouled area and the surface.

Self-cleaning test

The self-cleaning tests were performed by using iron oxide particles to mimic dirt contamination on the MPS surfaces. Superhydrophobic surfaces made of different materials, *i.e.*, PDMS, polyethylene (PE), and PP, with the same topology were used for comparison. The iron oxide (Fe_3O_4) particles were firstly spread on the tested surfaces and tapped gently to ensure that they have close contact with the surfaces. Water was then dropped onto the surfaces to remove the particles. To investigate the effect of particle size on the self-cleaning property of the tested surfaces, ~2-μm and ~200-nm iron oxide particles were employed as the mimetic dirt. Pining of water droplets on a tested surface was used as the evidence of a surface failing to self-clean.

Substrate adhesion tests

The substrate adhesion of MPS was characterized by the shear stress model. The tested substrate was sandwiched between two aluminum plates, and the interfaces were thermally bonded by a perfluoropolymer thin film. The bonded area was 25×20 mm^2. To realize the bonding, the sandwiched sample were laminated at 350 °C for 10 min and then cooled to room temperature. The bonding strength was measured with a tensiometer, where the stress was recorded as a function of the longitudinal extension regulated at a speed of 5 mm/min. After detached, the contact angle measurement, scan electron microscope (SEM) imaging, and X-ray photoelectron spectroscopy (XPS) were conducted to investigate the fracture interfaces.

The adhesion strength was further tested by using tape peeling and repeated folding. The peeling test used a pressure-sensitive rubbery adhesive (Blu Tack, Bostik), which can fill the texture of rough surfaces rather than only adhere to the very top of surface structures. After laminating with the tested surfaces under ~500 KPa for 5 min, the rubbery adhesive was peeled off slowly.

Folding test

A folding test was conducted to evaluate the material flexibility by the reciprocated folding model. The water repellence (θ^* and $\theta_{roll\text{-}off}$) was recorded after every 10,000 cycles to characterize the robustness of the sample.

Chemical and aging tests

The chemical robustness of the MPS was tested against gaseous corrosives, aging conditions, as well as other harsh environments. A commercial superhydrophobic spray (NeverWet) and a water-repelling textile were comparatively tested. To evaluate the robustness against gaseous corrosives, samples and corrosive chemicals were placed inside a sealed container, which was then evacuated to 90 KPa to generate a saturated corrosive gas atmosphere. The chemicals included 37% HCl, 25% $NH_3 \cdot H_2O$, 98% HNO_3, acetone, chloroform, and toluene, respectively. The duration for each test was 7 days. For the accelerated

aging test, samples were exposed to 254-nm UV radiation at 70 °C and 70% relative humidity. For the harsh environments test, fresh samples were exposed to ultrasonication (40 kHz) in the above chemicals for 1 h, 185-nm UV radiation for 7 days, air plasma for 30 min, and 200 °C heat for 7 days. The water repellence (θ* and $\theta_{roll\text{-}off}$) of these samples was measured during and after these tests for determining durability.

Thermal stability

To investigate the thermal stability of the MPS, we heated a superhydrophobic MPS, a high-quality commercial water-repelling spray (NeverWet), and a commercial water-repelling textile at 200 °C for one day. We found that the color of the commercial products faded seriously, and their surfaces became hydrophilic, whereas the MPS remained superhydrophobic. After being heated at 250 °C for one week, the MPS superhydrophobic surface was still intact.

REFERENCES

1. Liu, M., Wang, S., and Jiang, L. (2017). Nature-inspired superwettability systems. Nat. Rev. Mater. ***2***, 17036.
2. Ivanova, E.P., Hasan, J., Webb, H.K., et al. (2012). Natural bactericidal surfaces: Mechanical rupture of pseudomonas aeruginosa cells by cicada wings. Small ***8***, 2489-2494.
3. Helbig, R., Nickerl, J., Neinhuis, C., and Werner, C. (2011). Smart skin patterns protect springtails. PLoS One ***6***, e25105.
4. Feng, L., Zhang, Y., Xi, J., et al. (2008). Petal effect: a superhydrophobic state with high adhesive force. Langmuir ***24***, 4114-4119.
5. Bird, J.C., Dhiman, R., Kwon, H.-M., and Varanasi, K.K. (2013). Reducing the contact time of a bouncing drop. Nature ***503***, 385-388.
6. Liu, Y., Moevius, L., Xu, X., et al. (2014). Pancake bouncing on superhydrophobic surfaces. Nat. Phys. ***10***, 515-519.
7. Tan, Y., Hu, B., Chu, Z., and Wu, W. (2019). Bioinspired superhydrophobic papillae with tunable adhesive force and ultralarge liquid capacity for microdroplet manipulation. Adv. Funct. Mater. ***29***, 1900266.
8. Feng, S., Zhu, P., Zheng, H., et al. (2021). Three-dimensional capillary ratchet-induced liquid directional steering. Science ***373***, 1344-1348.
9. Hu, S., Cao, X., Reddyhoff, T., et al. (2022). Pneumatic programmable superrepellent surfaces. Droplet ***1***, 48-55.
10. Zhu, P., Kong, T., Tang, X., and Wang, L. (2017). Well-defined porous membranes for robust omniphobic surfaces via microfluidic emulsion templating. Nat. Commun. ***8***, 15823.

11. Hensel, R., Finn, A., Helbig, R., et al. (2014). Biologically Inspired Omniphobic Surfaces by Reverse Imprint Lithography. Adv. Mater. ***26***, 2029-2033.
12. Li, X., Zhang, J., Wang, X., et al. (2022). Bio-inspired spontaneous splitting of underwater bubbles along a superhydrophobic open pathway without perturbation. Droplet ***1***, 65-75.
13. Wu, S., Du, Y., Alsaid, Y., et al. (2020). Superhydrophobic photothermal icephobic surfaces based on candle soot. Proc. Natl. Acad. Sci. U. S. A. ***117***, 11240-11246.
14. Yao, Y., Zhao, T.Y., Machado, C., et al. (2020). Frost-free zone on macrotextured surfaces. Proc. Natl. Acad. Sci. U. S. A. ***117***, 6323-6329.
15. Gurumukhi, Y., Chavan, S., Sett, S., et al. (2020). Dynamic defrosting on superhydrophobic and biphilic surfaces. Matter ***3***, 1178-1195.
16. Pan, S., Kota, A.K., Mabry, J.M., and Tuteja, A. (2013). Superomniphobic surfaces for effective chemical shielding. J. Am. Chem. Soc. ***135***, 578-581.
17. Lee, C., and Kim, C.J. (2011). Underwater restoration and retention of gases on superhydrophobic surfaces for drag reduction. Phys. Rev. Lett. ***106***, 014502.
18. Xu, M., Sun, G., and Kim, C.J. (2014). Infinite lifetime of underwater superhydrophobic states. Phys. Rev. Lett. ***113***, 136103.
19. Zhang, W., Shi, Z., Zhang, F., et al. (2013). Superhydrophobic and superoleophilic PVDF membranes for effective separation of water-in-oil emulsions with high flux. Adv. Mater. ***25***, 2071-2076.
20. Gao, X., Zhou, J., Du, R., et al. (2016). Robust superhydrophobic foam: a graphdiyne-based hierarchical architecture for oil/water separation. Adv. Mater. ***28***, 168-173.
21. Li, G., Hong, G., Dong, D., et al. (2018). Multiresponsive graphene-aerogel-directed phase-change smart Fibers. Adv. Mater. ***30***, 1801754.
22. Tesler, A.B., Kim, P., Kolle, S., et al. (2015). Extremely durable biofouling-resistant metallic surfaces based on electrodeposited nanoporous tungstite films on steel. Nat. Commun. ***6***, 8649.
23. Privett, B.J., Youn, J., Hong, S.A., et al. (2011). Antibacterial fluorinated silica colloid superhydrophobic surfaces. Langmuir ***27***, 9597-9601.
24. Deng, X., Mammen, L., Butt, H.J., and Vollmer, D. (2012). Candle soot as a template for a transparent robust superamphiphobic coating. Science ***335***, 67-70.
25. Lu, Y., Sathasivam, S., Song, J., et al. (2015). Robust self-cleaning surfaces that function when exposed to either air or oil. Science ***347***, 1132-1135.
26. Peng, C., Chen, Z., and Tiwari, M.K.M.K. (2018). All-organic superhydrophobic coatings with mechanochemical robustness and liquid impalement resistance. Nat. Mater. ***17***, 355-360.
27. Pan, S., Guo, R., Björnmalm, M., et al. (2018). Coatings super-repellent to ultralow surface tension liquids. Nat. Mater. ***17***, 1040-1047.
28. Li, Z., Cao, M., Li, P., et al. (2019). Surface-embedding of functional micro-/nanoparticles for achieving versatile superhydrophobic interfaces. Matter ***1***, 661-673.
29. Wang, D., Sun, Q., Hokkanen, M.J., et al. (2020). Design of robust superhydrophobic surfaces. Nature ***582***, 55-59.
30. Kondrashov, V., and Rühe, J. (2014). Microcones and nanograss: Toward mechanically robust superhydrophobic surfaces. Langmuir ***30***, 4342-4350.
31. Liu, T.L., and Kim, C.-J.C. (2014). Turning a surface superrepellent even to completely wetting liquids. Science ***346***, 1096-1100.
32. Yun, G.T., Jung, W.B., Oh, M.S., et al. (2018). Springtail-inspired superomniphobic surface with extreme pressure resistance. Sci. Adv. ***4***, eaat4978.
33. Gonzalez-Avila, S.R., Nguyen, D.M., Arunachalam, S., et al. (2020). Mitigating cavitation erosion using biomimetic gas-entrapping microtextured surfaces (GEMS). Sci. Adv. ***6***, eaax6192.

34. Domingues, E.M., Arunachalam, S., Nauruzbayeva, J., and Mishra, H. (2018). Biomimetic coating-free surfaces for long-term entrapment of air under wetting liquids. Nat. Commun. ***9***, 3606.
35. Mates, J.E., Bayer, I.S., Palumbo, J.M., et al. (2015). Extremely stretchable and conductive water-repellent coatings for low-cost ultra-flexible electronics. Nat. Commun. ***6***, 8874.
36. Li, W., Yu, M., Sun, J., et al. (2019). Crack engineering for the construction of arbitrary hierarchical architectures. Proc. Natl. Acad. Sci. U. S. A. ***116***, 23909-23914.
37. Zhang, L., Zhou, A.G., Sun, B.R., et al. (2021). Functional and versatile superhydrophobic coatings via stoichiometric silanization. Nat. Commun. ***12***, 982.
38. Verho, T., Bower, C., Andrew, P., et al. (2011). Mechanically durable superhydrophobic surfaces. Adv. Mater. ***23***, 673-678.
39. Schutzius, T.M., Jung, S., Maitra, T., et al. (2015). Spontaneous droplet trampolining on rigid superhydrophobic surfaces. Nature ***527***, 82-85.
40. Dhyani, A., Wang, J., Halvey, A.K., et al. (2021). Design and applications of surfaces that control the accretion of matter. Science ***373***, 294.
41. Zheng, Q.S., Yu, Y., and Zhao, Z.H. (2005). Effects of hydraulic pressure on the stability and transition of wetting modes of superhydrophobic surfaces. Langmuir ***21***, 12207-12212.
42. Panter, J.R., Gizaw, Y., and Kusumaatmaja, H. (2019). Multifaceted design optimization for superomniphobic surfaces. Sci. Adv. ***5***, eaav7328.
43. Carpinteri, A., and Pugnø, N. (2005). Are scaling laws on strength of solids related to mechanics or to geometry? Nat. Mater. ***4***, 421-423.
44. Cranford, S.W., Tarakanova, A., Pugno, N.M., and Buehler, M.J. (2012). Nonlinear material behaviour of spider silk yields robust webs. Nature ***482***, 72-76.
45. Ren, K., Dai, W., Zhou, J., et al. (2011). Whole-Teflon microfluidic chips. Proc. Natl. Acad. Sci. U. S. A. ***108***, 8162-8166.
46. Krumpfer, J.W., Bian, P., Zheng, P., et al. (2011). Contact angle hysteresis on superhydrophobic surfaces: An ionic liquid probe fluid offers mechanistic insight. Langmuir ***27***, 2166-2169.
47. Carré, A., Gastel, J.C., and Shanahan, M.E.R. (1996). Viscoelastic effects in the spreading of liquids. Nature.
48. Kleeman, M.J., and Cass, G.R. (1998). Source contributions to the size and composition of urban particulate air pollution. Atmos. Environ. ***32***, 2803-2816.
49. Shi, S., Lv, C., and Zheng, Q. (2019). Drop impact on two-tier monostable superrepellent surfaces. ACS Appl. Mater. Inter. ***11***, 43698-43707.
50. Nilsson, M.a., Daniello, R.J., and Rothstein, J.P. (2010). A novel and inexpensive technique for creating superhydrophobic surfaces using Teflon and sandpaper. J. Phys. D: Appl. Phys. ***43***, 045301.

1. Liu, M., Wang, S., and Jiang, L. (2017). Nature-inspired superwettability systems. Nature Reviews Materials ***2***, 17036.
2. Ivanova, E.P., Hasan, J., Webb, H.K., et al. (2012). Natural bactericidal surfaces: Mechanical rupture of pseudomonas aeruginosa cells by cicada wings. Small ***8***, 2489-2494.
3. Helbig, R., Nickerl, J., Neinhuis, C., and Werner, C. (2011). Smart skin patterns protect springtails. PLoS ONE ***6***, e25105.
4. Feng, L., Zhang, Y., Xi, J., et al. (2008). Petal effect: a superhydrophobic state with high adhesive force. Langmuir ***24***, 4114-4119.
5. Bird, J.C., Dhiman, R., Kwon, H.-M., and Varanasi, K.K. (2013). Reducing the contact time of a bouncing drop. Nature ***503***, 385-388.
6. Liu, Y., Moevius, L., Xu, X., et al. (2014). Pancake bouncing on superhydrophobic surfaces. Nature Physics ***10***, 515-519.

7. Tan, Y., Hu, B., Chu, Z., and Wu, W. (2019). Bioinspired superhydrophobic papillae with tunable adhesive force and ultralarge liquid capacity for microdroplet manipulation. Advanced Functional Materials ***29***, 1900266-1900266.
8. Feng, S., Zhu, P., Zheng, H., et al. (2021). Three-dimensional capillary ratchet-induced liquid directional steering. Science ***373***, 1344-1348.
9. Hu, S., Cao, X., Reddyhoff, T., et al. (2022). Pneumatic programmable superrepellent surfaces. Droplet ***1***, 48-55.
10. Zhu, P., Kong, T., Tang, X., and Wang, L. (2017). Well-defined porous membranes for robust omniphobic surfaces via microfluidic emulsion templating. Nature Communications ***8***, 1-10.
11. Hensel, R., Finn, A., Helbig, R., et al. (2014). Biologically Inspired Omniphobic Surfaces by Reverse Imprint Lithography. Advanced Materials ***26***, 2029-2033.
12. Li, X., Zhang, J., Wang, X., et al. (2022). Bio-inspired spontaneous splitting of underwater bubbles along a superhydrophobic open pathway without perturbation. Droplet ***1***, 65-75.
13. Wu, S., Du, Y., Alsaid, Y., et al. (2020). Superhydrophobic photothermal icephobic surfaces based on candle soot. Proceedings of the National Academy of Sciences of the United States of America ***117***, 11240-11246.
14. Yao, Y., Zhao, T.Y., Machado, C., et al. (2020). Frost-free zone on macrotextured surfaces. Proceedings of the National Academy of Sciences of the United States of America ***117***, 6323-6329.
15. Gurumukhi, Y., Chavan, S., Sett, S., et al. (2020). Dynamic defrosting on superhydrophobic and biphilic surfaces. Matter ***3***, 1178-1195.
16. Pan, S., Kota, A.K., Mabry, J.M., and Tuteja, A. (2013). Superomniphobic surfaces for effective chemical shielding. Journal of the American Chemical Society ***135***, 578-581.
17. Lee, C., and Kim, C.J. (2011). Underwater restoration and retention of gases on superhydrophobic surfaces for drag reduction. Physical Review Letters ***106***, 014502-014502.
18. Xu, M., Sun, G., and Kim, C.J. (2014). Infinite lifetime of underwater superhydrophobic states. Physical Review Letters ***113***, 136103.
19. Zhang, W., Shi, Z., Zhang, F., et al. (2013). Superhydrophobic and superoleophilic PVDF membranes for effective separation of water-in-oil emulsions with high flux. Advanced Materials ***25***, 2071-2076.
20. Gao, X., Zhou, J., Du, R., et al. (2016). Robust superhydrophobic foam: a graphdiyne-based hierarchical architecture for oil/water separation. Advanced Materials ***28***, 168-173.
21. Li, G., Hong, G., Dong, D., et al. (2018). Multiresponsive graphene-aerogel-directed phase-change smart Fibers. Advanced Materials ***30***, 1801754.
22. Tesler, A.B., Kim, P., Kolle, S., et al. (2015). Extremely durable biofouling-resistant metallic surfaces based on electrodeposited nanoporous tungstite films on steel. Nature Communications ***6***, 8649.
23. Privett, B.J., Youn, J., Hong, S.A., et al. (2011). Antibacterial fluorinated silica colloid superhydrophobic surfaces. Langmuir ***27***, 9597-9601.
24. Deng, X., Mammen, L., Butt, H.J., and Vollmer, D. (2012). Candle soot as a template for a transparent robust superamphiphobic coating. Science ***335***, 67-70.
25. Lu, Y., Sathasivam, S., Song, J., et al. (2015). Robust self-cleaning surfaces that function when exposed to either air or oil. Science ***347***, 1132-1135.
26. Peng, C., Chen, Z., and Tiwari, M.K.M.K. (2018). All-organic superhydrophobic coatings with mechanochemical robustness and liquid impalement resistance. Nature Materials ***17***, 355-360.
27. Pan, S., Guo, R., Björnmalm, M., et al. (2018). Coatings super-repellent to ultralow surface tension liquids. Nature Materials ***17***, 1040-1047.
28. Li, Z., Cao, M., Li, P., et al. (2019). Surface-embedding of functional micro-/nanoparticles for achieving versatile superhydrophobic interfaces. Matter ***1***, 661-673.
29. Wang, D., Sun, Q., Hokkanen, M.J., et al. (2020). Design of robust superhydrophobic surfaces. Nature ***582***, 55-59.

30. Kondrashov, V., and Rühe, J. (2014). Microcones and nanograss: Toward mechanically robust superhydrophobic surfaces. Langmuir ***30***, 4342-4350.
31. Liu, T.L., and Kim, C.-J.C. (2014). Turning a surface superrepellent even to completely wetting liquids. Science ***346***, 1096-1100.
32. Yun, G.T., Jung, W.B., Oh, M.S., et al. (2018). Springtail-inspired superomniphobic surface with extreme pressure resistance. Science Advances ***4***, eaat4978.
33. Gonzalez-Avila, S.R., Nguyen, D.M., Arunachalam, S., et al. (2020). Mitigating cavitation erosion using biomimetic gas-entrapping microtextured surfaces (GEMS). Science Advances ***6***, eaax6192.
34. Domingues, E.M., Arunachalam, S., Nauruzbayeva, J., and Mishra, H. (2018). Biomimetic coating-free surfaces for long-term entrapment of air under wetting liquids. Nature Communications ***9***, 3606.
35. Mates, J.E., Bayer, I.S., Palumbo, J.M., et al. (2015). Extremely stretchable and conductive water-repellent coatings for low-cost ultra-flexible electronics. Nature Communications 2015 6:1 ***6***, 8874.
36. Li, W., Yu, M., Sun, J., et al. (2019). Crack engineering for the construction of arbitrary hierarchical architectures. Proceedings of the National Academy of Sciences of the United States of America ***116***, 23909-23914.
37. Zhang, L., Zhou, A.G., Sun, B.R., et al. (2021). Functional and versatile superhydrophobic coatings via stoichiometric silanization. Nature Communications ***12***, 982.
38. Verho, T., Bower, C., Andrew, P., et al. (2011). Mechanically durable superhydrophobic surfaces. Advanced Materials ***23***, 673-678.
39. Schutzius, T.M., Jung, S., Maitra, T., et al. (2015). Spontaneous droplet trampolining on rigid superhydrophobic surfaces. Nature ***527***, 82-85.
40. Dhyani, A., Wang, J., Halvey, A.K., et al. (2021). Design and applications of surfaces that control the accretion of matter. Science ***373***, 294.
41. Zheng, Q.S., Yu, Y., and Zhao, Z.H. (2005). Effects of hydraulic pressure on the stability and transition of wetting modes of superhydrophobic surfaces. Langmuir ***21***, 12207-12212.
42. Panter, J.R., Gizaw, Y., and Kusumaatmaja, H. (2019). Multifaceted design optimization for superomniphobic surfaces. Science Advances ***5***, eaav7328.
43. Carpinteri, A., and Pugnø, N. (2005). Are scaling laws on strength of solids related to mechanics or to geometry? Nature Materials ***4***, 421-423.
44. Cranford, S.W., Tarakanova, A., Pugno, N.M., and Buehler, M.J. (2012). Nonlinear material behaviour of spider silk yields robust webs. Nature ***482***, 72-76.
45. Ren, K., Dai, W., Zhou, J., et al. (2011). Whole-Teflon microfluidic chips. Proceedings of the National Academy of Sciences of the United States of America ***108***, 8162-8166.
46. Krumpfer, J.W., Bian, P., Zheng, P., et al. (2011). Contact angle hysteresis on superhydrophobic surfaces: An ionic liquid probe fluid offers mechanistic insight. Langmuir ***27***, 2166-2169.
47. Carré, A., Gastel, J.C., and Shanahan, M.E.R. (1996). Viscoelastic effects in the spreading of liquids. Nature.
48. Kleeman, M.J., and Cass, G.R. (1998). Source contributions to the size and composition of urban particulate air pollution. Atmospheric Environment ***32***, 2803-2816.
49. Shi, S., Lv, C., and Zheng, Q. (2019). Drop impact on two-tier monostable superrepellent surfaces. ACS applied materials & interfaces ***11***, 43698-43707.
50. Nilsson, M.a., Daniello, R.J., and Rothstein, J.P. (2010). A novel and inexpensive technique for creating superhydrophobic surfaces using Teflon and sandpaper. Journal of Physics D: Applied Physics ***43***, 045301.

ACKNOWLEDGMENTS

This work was supported by the National Natural Science Foundation of China (51773173, 81973288), Hong Kong RGC (T12-201/20-R, 12301720, 12202422, RMGS 2020_4_01), HKBU SKLEBA SKL-CRF (SKLP_1718_P01), SZSTC (SGDX20190816230207535), the FET Open (Boheme) grant No. 863179, and the Shanghai Pujiang Program 22PJ1406100. We acknowledge the Surface Analysis & Material Characterization Laboratory of HKBU for the SEM characterization and Nanosystem Fabrication Facility (NFF) of HKUST for the 3D laser lithography fabrication.

AUTHOR CONTRIBUTIONS

K. N. R. and H. K. W. conceived the idea and led the project. W. B. L., K. N. R, and H. K. W. designed the experiments. W. B. L., C. W. C., Z. Y. L., S. Y. S., S. Y. C., H. S., Z. Y. L., Y. S. W., and C. H. conducted the experiments and analyzed the data. N. M. P. built the theoretical model. W. B. L., N.M.P., R.N.Z., H.K.W., and K. N. R. wrote the paper. All authors discussed the results and commented on the manuscript.

DECLARATION OF INTERESTS

The authors declare no competing interests.

SUPPLEMENTAL INFORMATION

It can be found online at……

LEAD CONTACT WEBSITE

https://renkangning.wixsite.com/rengroup

Figures and Tables

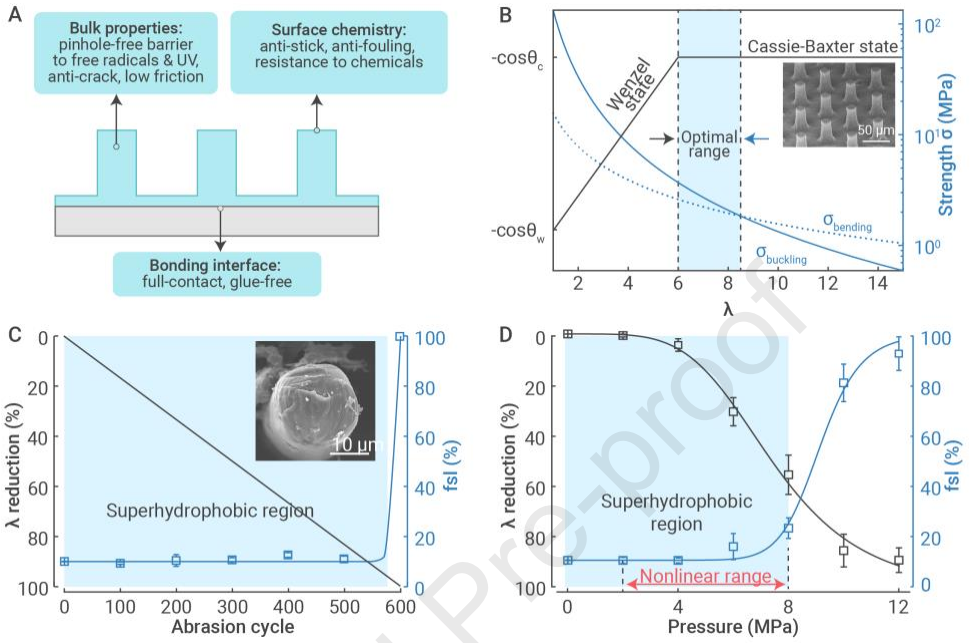

Figure 1. The MPS strategy coupling wetting and mechanical stability (A) A pillar model showing the MPS design for promoting outstanding chemical resistance, substrate adhesion, and eco-friendliness. (B) Change of theoretical wetting stability and influence of theoretical strength against buckling and bending of the pillar array as a function of the pillar slenderness λ. The light blue region indicates the optimal range for achieving both wetting and mechanical stability. (C and D) Experimental validation of the pillar strength based on a pillar array (λ_0 = 8) by plotting the change of the slenderness λ and liquid-solid contact fraction f_{ls} of the pillar array during repeated abrasion (C), and pressing under different apparent pressures (D), respectively. Data are mean ± s.d. from at least five independent measurements.

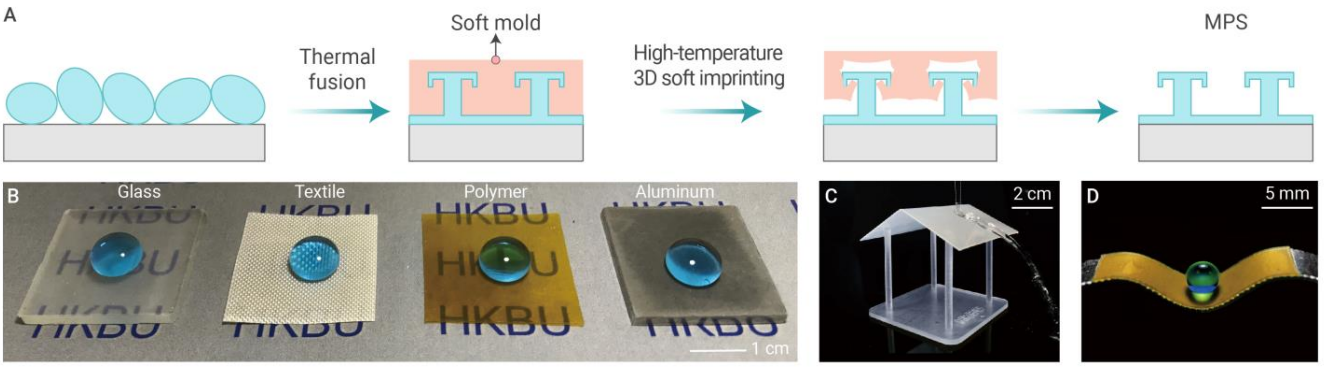

Figure 2. MPS Fabrication (A) Schematic illustration of fabrication method consisting of thermal fusion and high-temperature 3D soft imprinting. The method enables outstanding 3D topological controllability, substrate adhesion, and scale-up capability. (B-D) Photographs of MPS biomimetic materials, including coatings on diverse substrates (e.g., glass, textile, PI, and aluminum) (B), a small shed made of a self-supporting superhydrophobic MPS membrane (C), and a composite tape stuck on a bent surface (D).

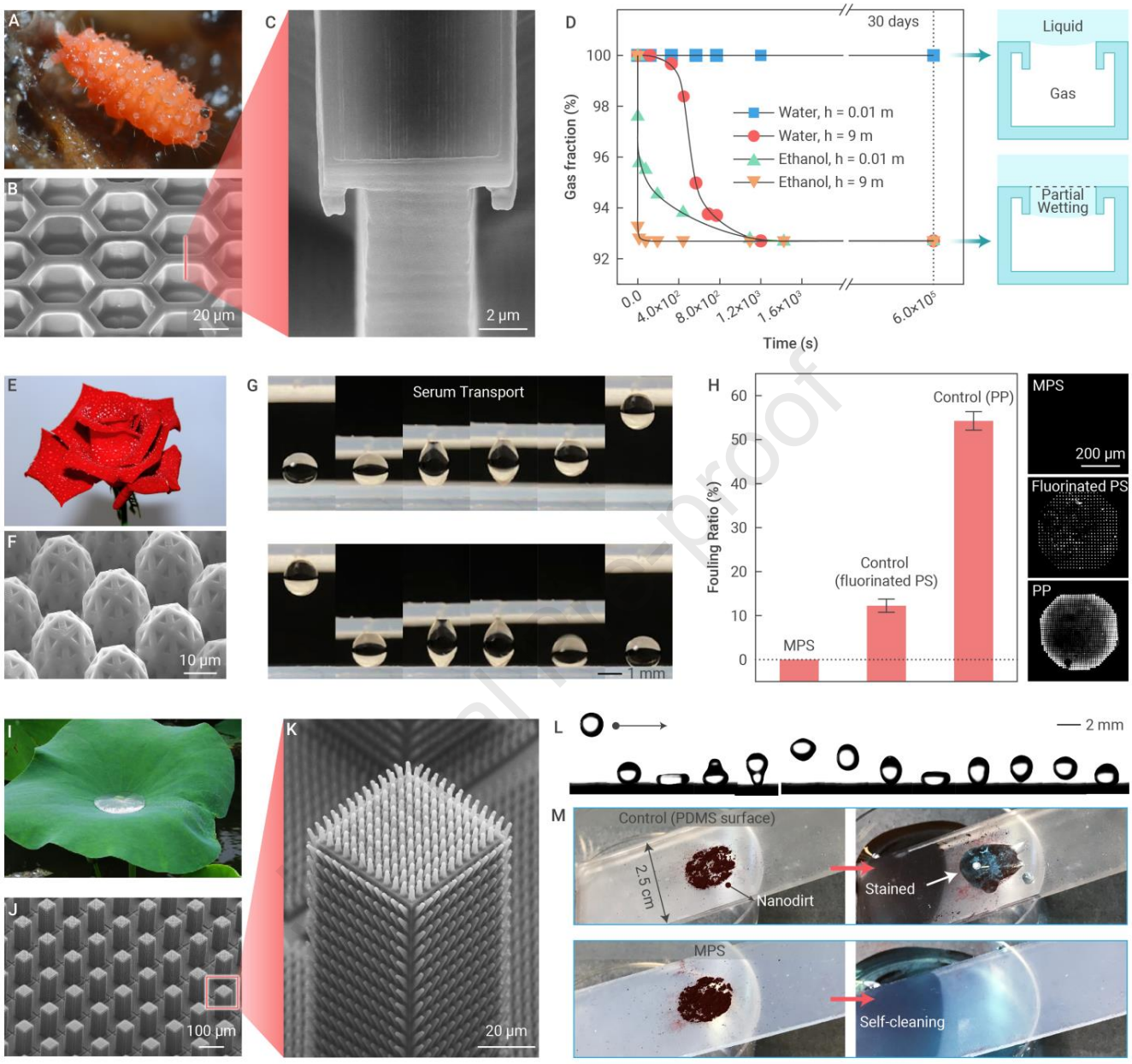

Figure 3. Topology-specific functionalities (A-D) MPS comprising cavities with doubly reentrants mimicking the skin structure of a springtail beetle for effective air trapping. (A) Optical image of a springtail. Image courtesy of Jan J. van Duinen (photographer). (B and C) SEM image of the cavity array (B) and the doubly reentrants (C). (D) The relationship between the fraction of entrapped air in the cavities and the immersion time. The scheme illustrates two models of liquid suspending at the first and second

reentrant, respectively. (E-H) MPS comprising micro protuberances mimicking the rose petal for low-fouling liquid droplet transportation. (E) Optical image of a rose flower with a high adhesion to water droplets. (f) SEM images of the MPS micro protuberances. (G) Optical images showing a droplet of serum transported between two MPS surfaces. (H) Measurement of the sample loss during transport. The MPS surface is free of observable fouling, while the counterparts, surfaces made of PP and fluorinated PS, suffer from serious fouling by bioanalytes. (I-M), Hierarchical MPS pillar array mimicking the lotus effect. (I) Image of a superhydrophobic lotus leaf. (J and K) SEM images showing the hierarchical topology of the pillar array (J) and the hierarchical unit (K). (L) Optical image showing the bouncing of a water droplet on the lotus-mimicking surface. (M), Representative images show the dirt removal tests. Only MPS surface showed self-cleaning property against nano-sized dirt (~200-nm in diameter), as compared with control surfaces (Supplementary Video 2). Data are mean ± s.d. from at least five independent measurements.

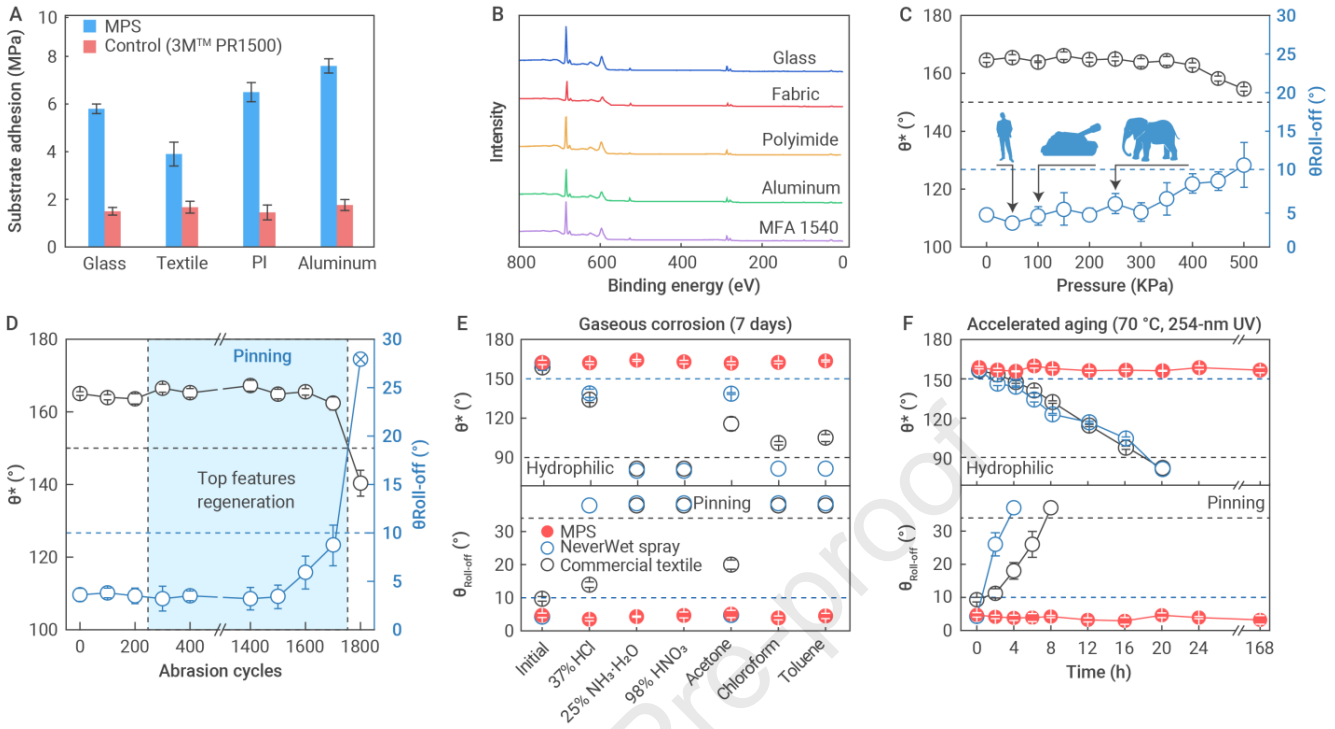

Figure. 4. Multipronged robustness (A and B) Substrate adhesion. (A) Adhesion strength of MPS with various substrates compared with the commercial glue 3M^{TM} PR1500. (B) XPS spectrum of the substrate surfaces after the perfluoropolymer layers were detached in the tests. The spectra are identical to that of MFA F1540. (C and D) Mechanical robustness. (C) Relationship between water repellence and apparent pressure applied to the surface in Figure 2E. For comparison, the ground pressure of an adult man, a military tank, and an elephant, respectively, were denoted in the insets. (D) Relationship between the water repellence of the surface in Figure 2E and abrasion cycles. (E and F) Chemical and aging robustness. (E) Water repellence of the MPS before and after treated with strong gaseous chemicals (acid, alkali, oxidant, and organic solvents) for 1 week. (F) Evolution of the water repellence of three superhydrophobic materials during accelerated aging. In C-F, the black and blue dash lines denote the boundaries of superhydrophobicity (θ^* > 150° and $\theta_{roll\text{-}off}$ <10°). In **E** and **F**, a commercial NeverWet spray and water-

repellence textile were also tested to provide reference index of the chemical and weathering stability. Data are mean ± s.d. from at least five independent measurements.

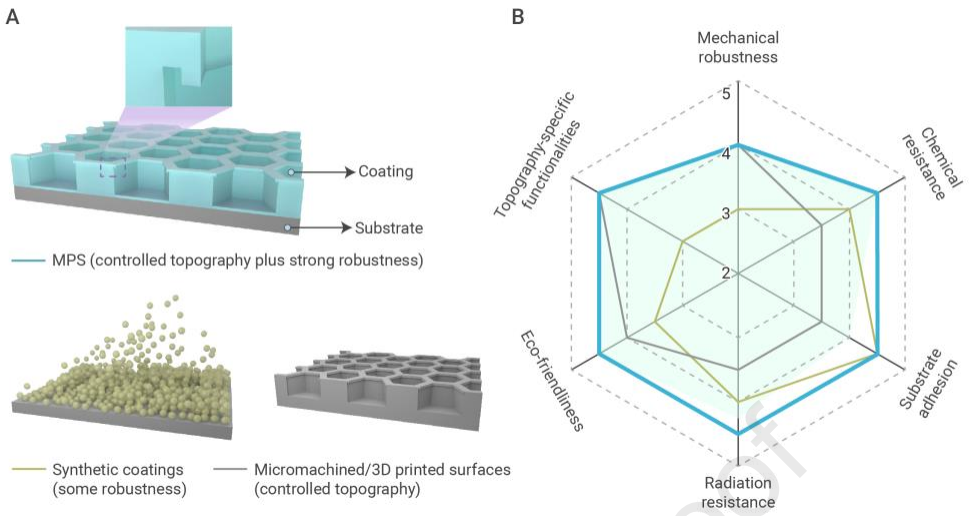

Figure. 5. MPS combines topological controllability and multilevel durability (A) illustration of two major groups of existing strategies (lower schematics), i.e., synthetic coatings and micromachined/3D printed surface, as well as MPS strategy (upper schematic) for preparing biomimetic surfaces. (B) A radar map showing the qualitative indexes of the characters of biomimetic coatings produced using different strategies (see references and rubrics in Table S2 and S3). The potential applications, e.g., anti-icing and drag reduction, require multipronged merits of biomimetic coatings (light green area). MPS biomimetic surfaces (light blue line) can fulfill the multipronged requirements, addressing the limitations of synthetic coatings (gray line) and micromachined/3D printed coatings (dark yellow line).

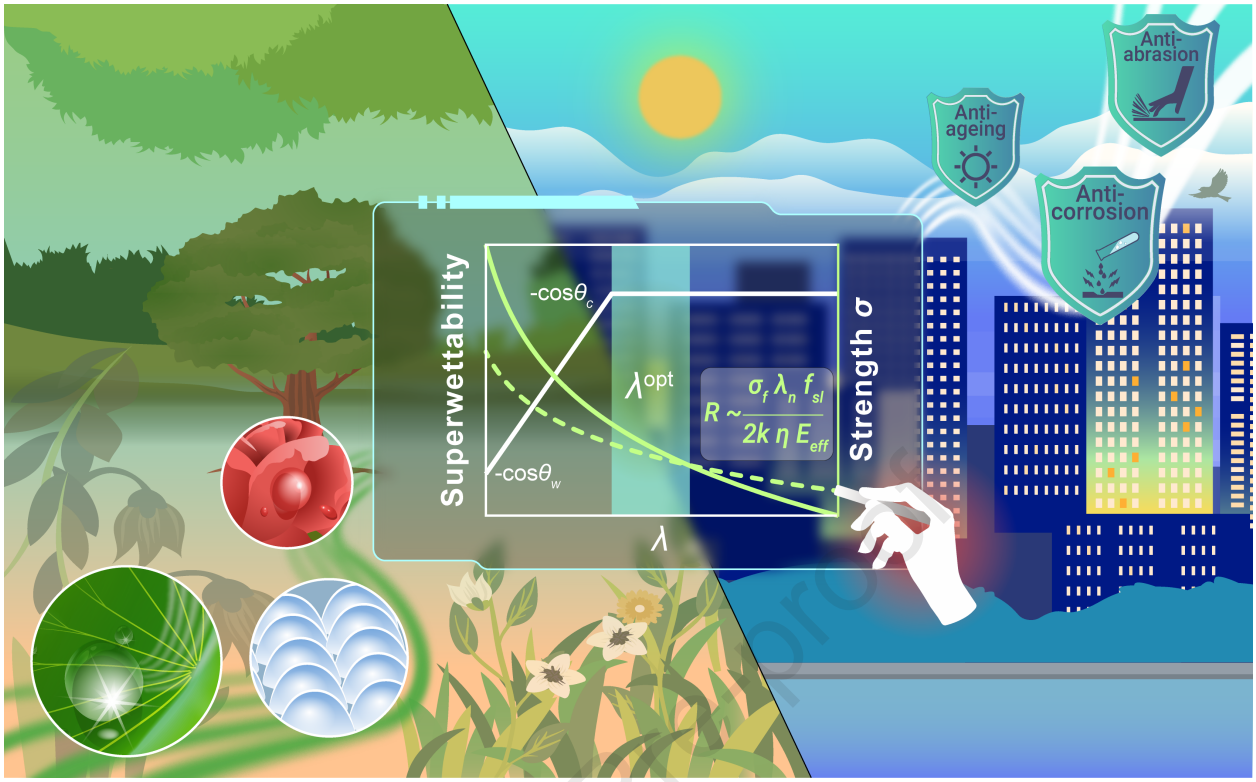

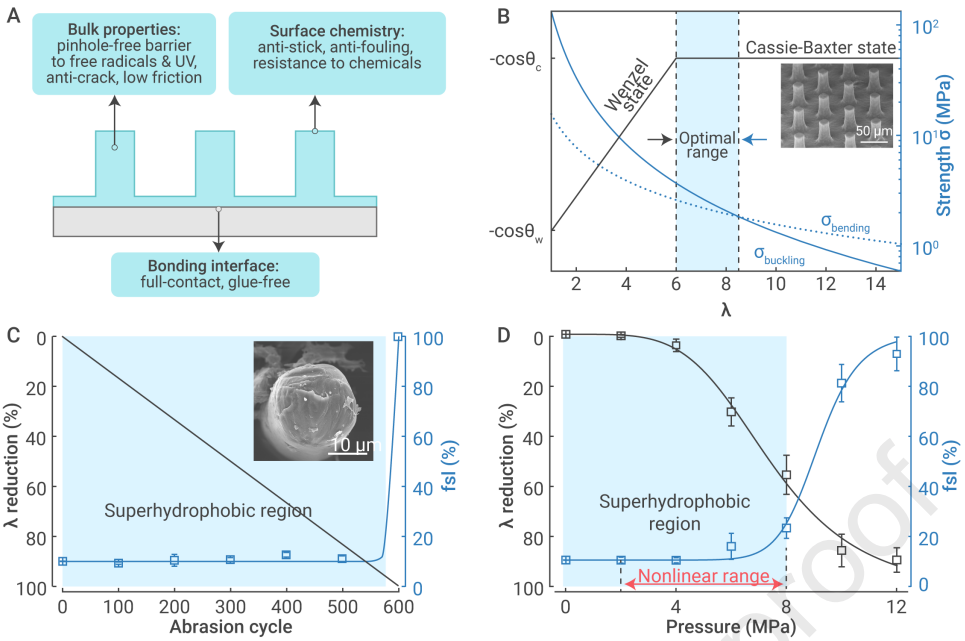

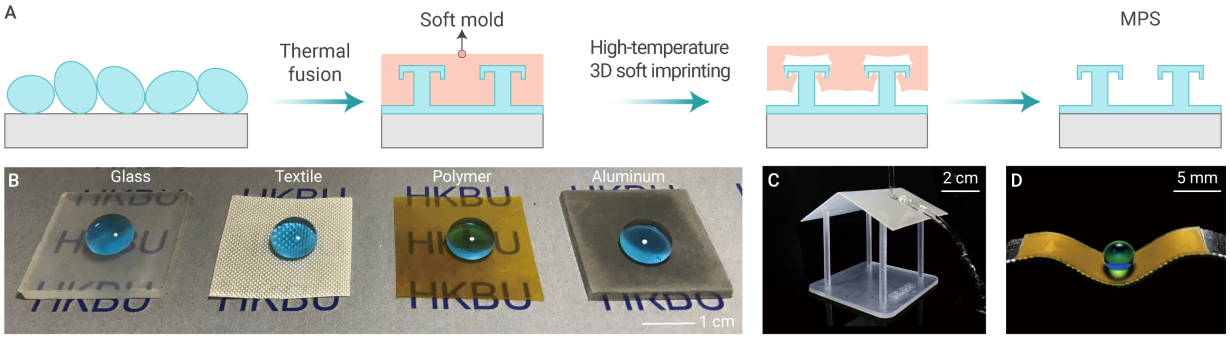

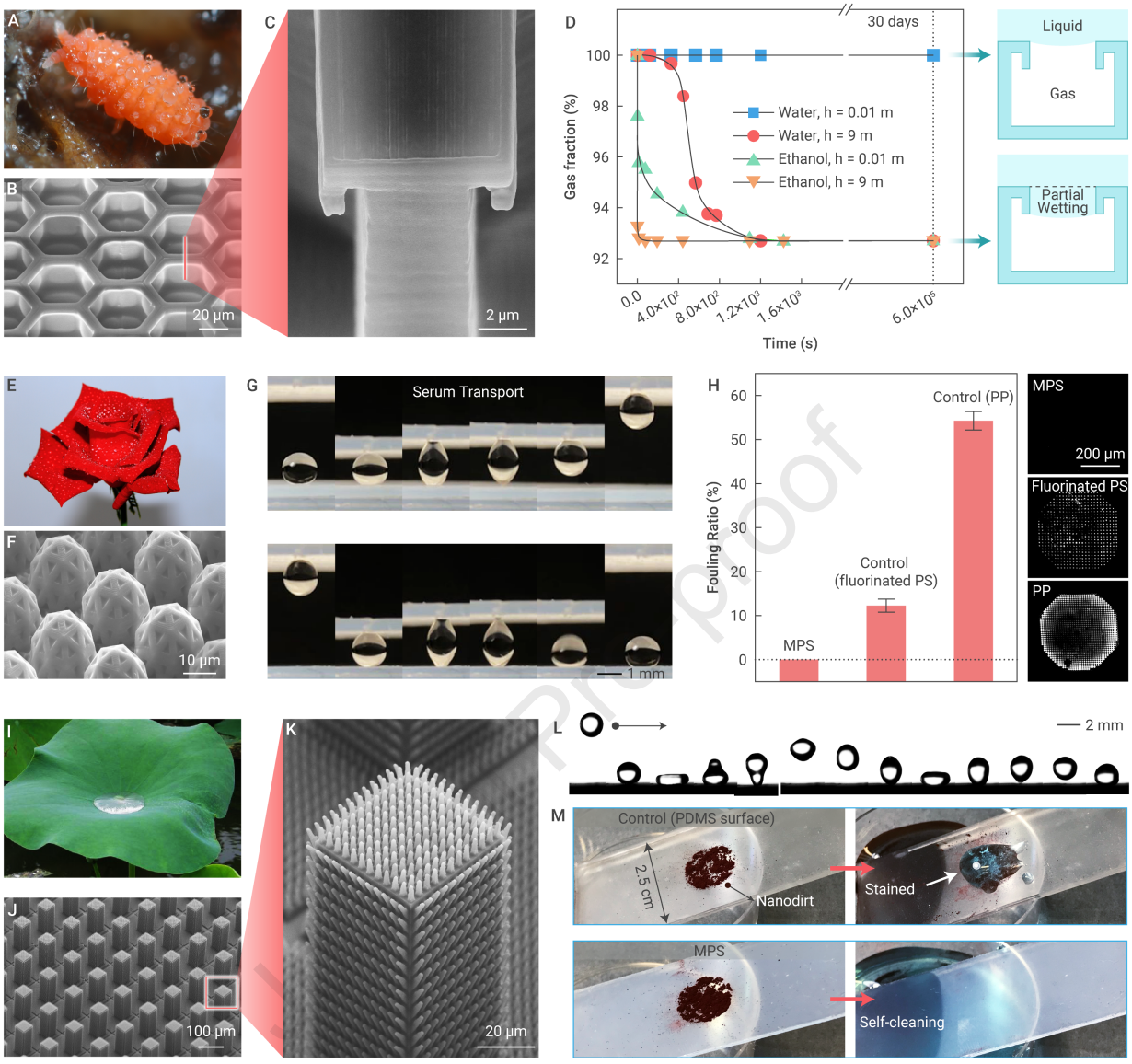

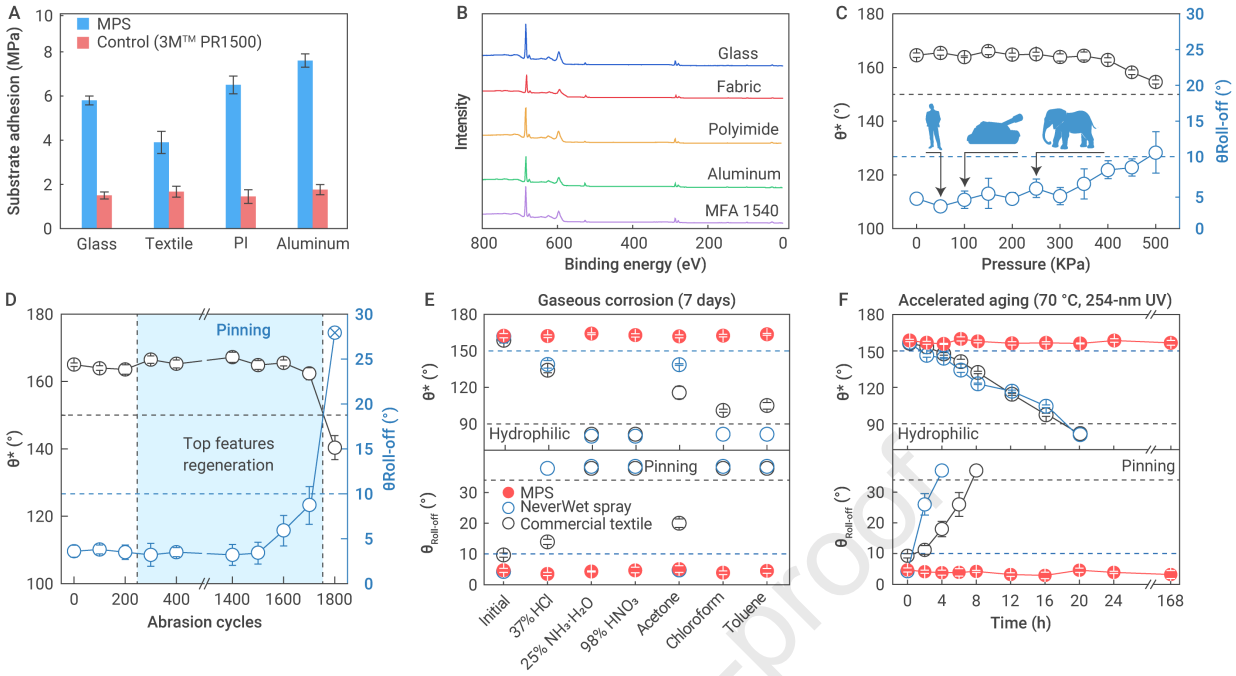

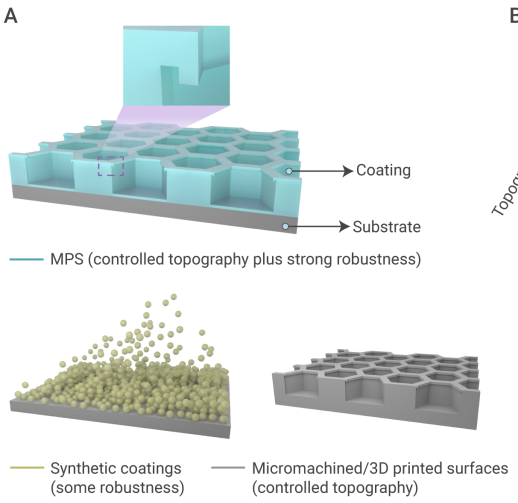

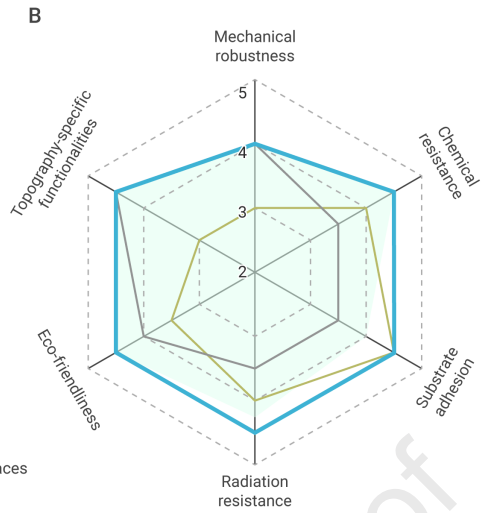

PUBLIC SUMMARY

- The monolithic perfluoropolymer surface (MPS) strategy enables biomimetic surfaces to combine geometric-material mechanics with topology-specific superwetting stability.
- The theoretical model predicted optimal structures and materials to realize simultaneously superwettability and ultradurability.
- The stability of the biomimetic surfaces was extended into a nonlinear range for further improving ultradurability.
- The MPS strategy helps to translate bioinspired surface principles into real-world applications.